Available online at www.sciencedirect.com

SciVerse ScienceDirect

Ceramics International 39 (2013) 6517–6526

CERAMICS INTERNATIONAL

www.elsevier.com/locate/ceramint

Stress enhanced TiO_2 nanowire growth on Ti–6Al–4V particles by thermal oxidation

M.M. Arafat[a], A.S.M.A. Haseeb[a,*], B. Dinan[b], S.A. Akbar[b]

[a]*Department of Mechanical Engineering, Faculty of Engineering, University of Malaya, 50603 Kuala Lumpur, Malaysia*
[b]*Department of Materials Science and Engineering, Ohio State University, 2041 College Road, Columbus, OH 43210, USA*

Received 10 November 2012; received in revised form 23 January 2013; accepted 26 January 2013
Available online 1 February 2013

Abstract

Titanium dioxide (TiO_2) nanowires were grown on Ti - 6wt% Al - 4wt% V (Ti64) particles by thermal oxidation. To investigate the effect of stress on nanowire growth, the particles were milled in a planetary ball mill prior to the thermal oxidation. Thermal oxidation of the Ti64 particles was carried out in a horizontal tube furnace in a controlled oxygen atmosphere in the temperature range of 700–900 °C. The oxygen concentration was varied from 20 ppm to 80 ppm in Ar atmosphere. Nanostructures were characterized by high resolution field emission scanning electron microscopy, energy dispersive spectroscopy and X-ray diffraction. TiO_2 nanowires grew on the surface of Ti64 particles and exhibited a square/rectangular cross sectional shape with thicknesses of 20–40 nm and lengths of 2–3 μm. Residual stress was found to play a significant role in nanowire growth. This was confirmed by growing TiO_2 nanowires on Ti64 alloy sheet with an induced stress gradient along its length. An improvement in nanowire coverage was observed in regions of high residual stress. A stress-induced growth mechanism is suggested to explain the confinement of nanowire growth to one dimension during thermal oxidation.

Keywords: Nanowire; Thermal oxidation; Growth mechanism; Ti64 alloy

1. Introduction

Nanostructured materials have attracted much attention in recent years for their unique properties, such as dimensional characteristics [1–3], enhanced surface area [4–6], quantum confinement [7,8] and electronic properties [9–11], which can differ significantly from their bulk counterparts. These opportunities have prompted research focused on the fabrication, characterization and application of nanostructured materials. Among these, nanostructured metal oxides are of particular interest for use in electronic devices due to their ease of fabrication, compatibility with other materials and processes, and relatively low cost [12].

More recently, one dimensional (1-D) TiO_2 nanostructures have shown promise in applications such as dye-sensitized solar cells [13–15], photocatalysis [16–18], photo-splitting of water [19,20], chemical sensors [21,22], photoelectrochemical cells [23], piezoelectronics [24] and bone implantation [25]. Several processes, including hydrothermal [26–28], electrospinning [29,30], anodization [31–34], nanocarving [21,35], and UV lithography with dry plasma etching [36], have been developed for the production of 1-D TiO_2 nanostructures. Wet chemical processes such as hydrothermal, electrospinning, and anodization require multiple chemical steps with proper control of processing variables. Moreover, most of the nanostructures produced by wet chemical route are amorphous, a distinct disadvantage for many engineering applications that require crystallinity. Solid state reaction processes such as UV lithography and dry plasma etching are complex and require high temperatures but result in crystalline nanostructures. Recently, a simple low-cost method to produce TiO_2 nanowires on commercially pure Ti and Ti alloys by thermal oxidation has been reported

*Corresponding author. Tel.: +60 3 7967 4598; fax: +60 3 7967 4448.
E-mail addresses: arafat_mahmood@siswa.um.edu.my (M.M. Arafat), haseeb@um.edu.my (A.S.M.A. Haseeb), dinan@matsceng.ohio-state.edu (B. Dinan), akbar.1@osu.edu (S.A. Akbar).

0272-8842/$ - see front matter © 2013 Elsevier Ltd and Techna Group S.r.l. All rights reserved.
http://dx.doi.org/10.1016/j.ceramint.2013.01.084

[37,38]. By annealing a Ti substrate in laboratory grade argon in the temperature range of 700–800 °C highly anisotropic TiO_2 nanostructures were grown. Nanowire growth by oxidation has several distinct advantages over many of the previously discussed techniques, the most significant of which being its low-cost and easy scalability for the large scale production of TiO_2 nanostructures [38].

The stress state of a metal prior to oxidation has been reported to be a critical component of nanowire formation by oxidation. A stress induced growth mechanism was proposed to explain the growth of CuO nanorods on Cu foil by thermal oxidation in air [39,40]. Formation of Cu_2O (simple cubic structure) underneath a CuO (monoclinic structure) layer during the thermal oxidation process creates a substantial stress at the interface. Diffusion of oxygen also accumulates stress at the interface of CuO/Cu_2O layers. When the stress exceeds a critical level, the oxide layer relaxes itself by the growth of 1-D nanostructures. The effects of residual stress on the formation of 1-D TiO_2 nanostructures by thermal oxidation were unknown. Here, we report for the first time the impact of residual stress on the formation of TiO_2 nanostructure grown by thermal oxidation. The process parameters for yielding a high coverage of TiO_2 nanowires on commercially available Ti - 6wt% Al - 4wt% V (Ti64) particles are also discussed. Based on the results obtained, a possible mechanism is presented to explain the growth of TiO_2 nanowires on Ti64.

2. Experimental procedure

As-received Ti64 particles (Powder Alloy Corporation, USA) were milled in a planetary ball mill (Retsch: PM 400-MA type) for up to 20 h at 250 rpm in ambient environment. Twenty four ZrO_2 balls (diameter: 1 cm and weight: 3 g) were used in the milling process. The ball to particle weight ratio was 10:1 and the size of the particles before and after milling was measured by a field emission scanning electron microscope (FESEM: Zeiss Ultra-60). After milling, the particles were cleaned in 30 vol% HCl for 30 min followed by cleaning in distilled water. A portion of the particles were characterized by an X-ray diffractometer (XRD: PANalytical Empyrean) using CuK_α radiation (0.1540598 nm) at 40 kV and 40 mA. To measure the stress in the particles, the XRD-$\sin^2\psi$ technique was employed at different tilt angles (ψ) ranging from 0° to 40° [41–43]. The incident X-ray beam was introduced through a window having a width of 0.5 in., 0.125° divergence slit and 0.0625° anti-scattering slit to contact the sample surface at a fixed incident angle Ω. A computer controlled Omega-goniometer was used for ψ tilt.

After cleaning and washing, Ti64 particles were dispersed in ethanol with 5 wt% of particle loading. Approximately 10 μL of suspension was taken by using a micropipette and slowly dropped on the alumina substrate. The substrate along with the particles was then placed in a quartz tube inside a horizontal tube furnace (Lindberg Blue M: TF55035COMA1). Before ramping the furnace temperature, the quartz tube was purged with Ar gas for 10 min to remove any contamination. The furnace was heated to 700–900 °C at a heating rate of 30 °C/min in a controlled oxidizing environment of Ar/O_2 mixture. The total flow rate of gas was maintained at 500 mL/min. The oxygen concentration was varied from 20 ppm to 80 ppm by using a digital mass flow controller (Sierra: C100L-CM-NR-2-0V1-SV1-PV2-V1). The particles were oxidized for 8 h and cooled inside the furnace in controlled atmosphere. To observe the surface morphology of the particles after oxidation, high resolution FESEM was employed. Elemental analysis was carried out with energy dispersive X-ray spectroscopy (EDS: EDAX-Genesis Utilities). The phase of the resulting nanostructured oxide was investigated by XRD techniques as previously described.

For stress gradient experiments, a Ti64 sheet (Good-Fellow Cambridge Limited, England) having a dimension of 25 mm × 3 mm × 1 mm was hammered at one end until the strain reached a value of 0.6 mm/mm. The other end was retained un-hammered. This created a gradual deformation on the Ti64 sheet from one end to the other. The sheet was cleaned using 50 vol% HCl followed by 50 vol% H_2SO_4 with a final cleaning in distilled water. The sheet was then oxidized under optimum conditions for 8 h. After oxidation, the surface morphology of the sheet was characterized using FESEM.

3. Results and discussion

As-received Ti64 particles were milled for up to 20 h in a planetary ball mill in ambient environment. Fig. 1 shows FESEM micrographs of Ti64 particles in as-received and milled conditions. The particle size was reduced progressively with an increase in milling time. From this point forward, the milling time will be used to designate Ti64 particles. For example, as-received Ti64 particles will be represented as 'Ti64—0 h', while particles subjected to 2, 5, 10, 15 and 20 h of milling will be represented as Ti64—2 h, Ti64—5 h, Ti64—10 h, Ti64—15 h and Ti64—20 h, respectively.

The distribution and average size of the particles were measured from FESEM images at 100× magnification using the linear intercept method and are shown in Fig. 2. For each condition, a total of 330 particles were used to evaluate the distribution and average particle size. With the increase in milling time, the peak particle size was reduced and the distribution became narrower. Fig. 2(b) shows the effect of milling time on the average particle size. The average size of the Ti64—0 h particles was 226.4 μm which reduced to 15.15 μm after 20 h of milling. The rate of size reduction decreased with increasing milling time (Fig. 2(b)).

To optimize conditions for the growth of nanowires on Ti64 particles the following strategy was adopted. First, the oxygen concentration, milling condition and oxidation time remained constant while the oxidation temperature was varied. The Ti64–0 h particles were subjected to 40 ppm of oxygen for 8 h in the temperature range of 700–900 °C. Nanowire growth occurred at the lowest test

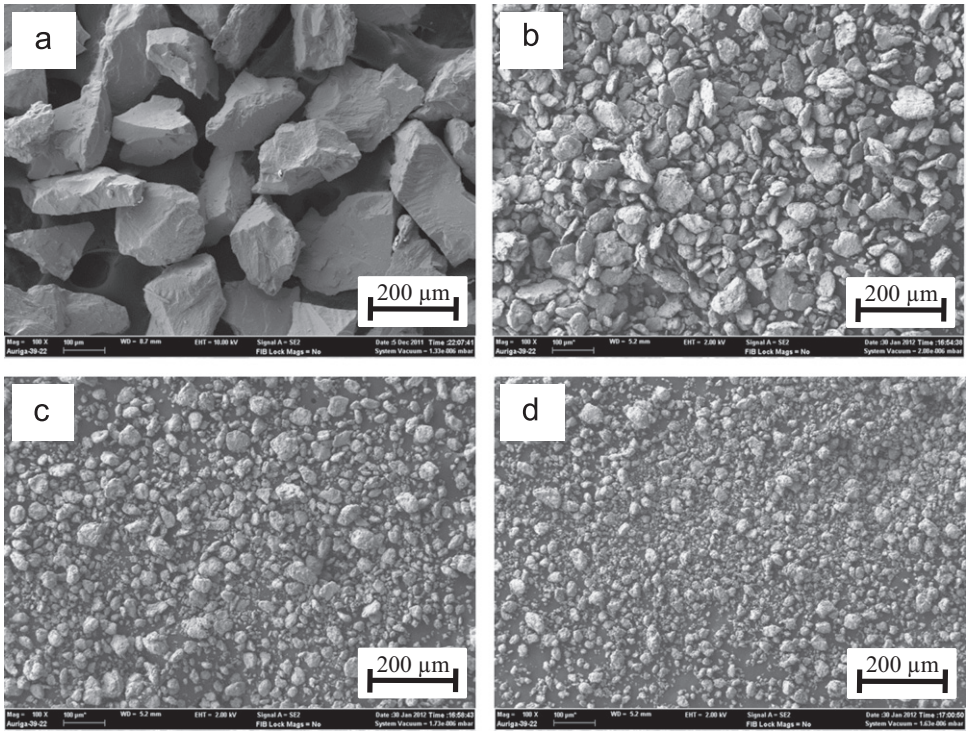

Fig. 1. FESEM micrograph of Ti64 particles after different milling time in hours: (a) Ti64—0 h, (b) Ti64—10 h, (c) Ti64—15 h and (d) Ti64—20 h.

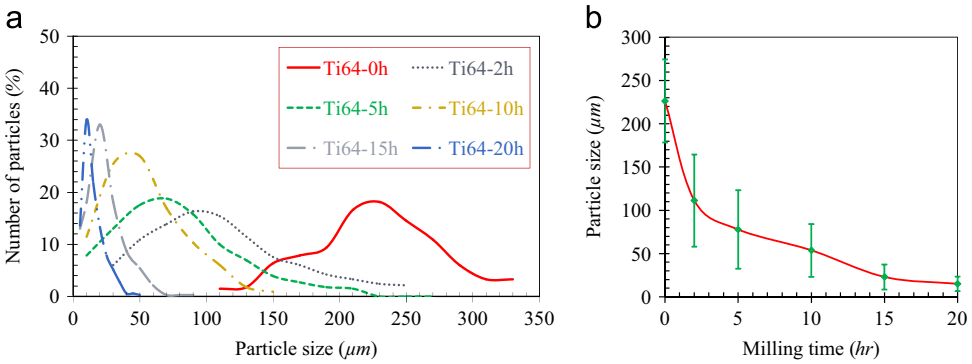

Fig. 2. (a) Distribution of particle size at different milling hours and (b) effect of milling time on average particle size.

temperature of 700 °C (Fig. 3(a)). As the temperature increased to 750°C, the coverage of nanowires increased (Fig. 3(b)). At 850 °C, faceted rods (approximately 1 µm in diameter) as well as some nanowires were observed (Fig. 3(c)). At 900 °C no nanowires were found on the Ti64 particles, only faceted grains were observed (Fig. 3(d)). These observations are consistent with the reported literature [37,38]. It has been previously reported that at low temperature, the oxidation reaction is driven by anisotropy with preferential growth on certain crystal faces which leads to the formation of nanowires. This anisotropy decreases at higher temperatures (800–900 °C), promoting growth on other surfaces, leading to increased wire diameters and the formation of facetted crystals.

The effect of oxygen concentration on nanowire growth was also investigated. The temperature, milling condition and oxidation time remained constant; only the oxygen concentration varied. Fig. 4 shows FESEM micrographs of Ti64—0 h particles after thermal oxidation at 750 °C with varying oxygen concentrations ranging from 20 ppm to 80 ppm. At low oxygen concentrations (20 ppm) no nanowire growth was observed (Fig. 4(a)). Similarly, at higher oxygen concentration (80 ppm) nanowire growth was not observed (Fig. 4(d)). Nanowires formed only in the range of 40–60 ppm of oxygen as observed in Fig. 4(b) and (c). Close examination of the micrographs indicates that nanowire coverage increased in the 40 ppm oxygen environment.

To investigate the effect of milling, Ti64 particles were subjected to different durations of milling prior to oxidation at 750 °C for 8 h in 40 ppm oxygen. Nanowires formed on all samples with varying coverage as shown in Fig. 5. The lowest coverage of nanowires was observed on the Ti64—0 h sample (Fig. 5(a)). The coverage increased with increased milling time (Fig. 5(b)–(d)). The highest coverage of nanowires was

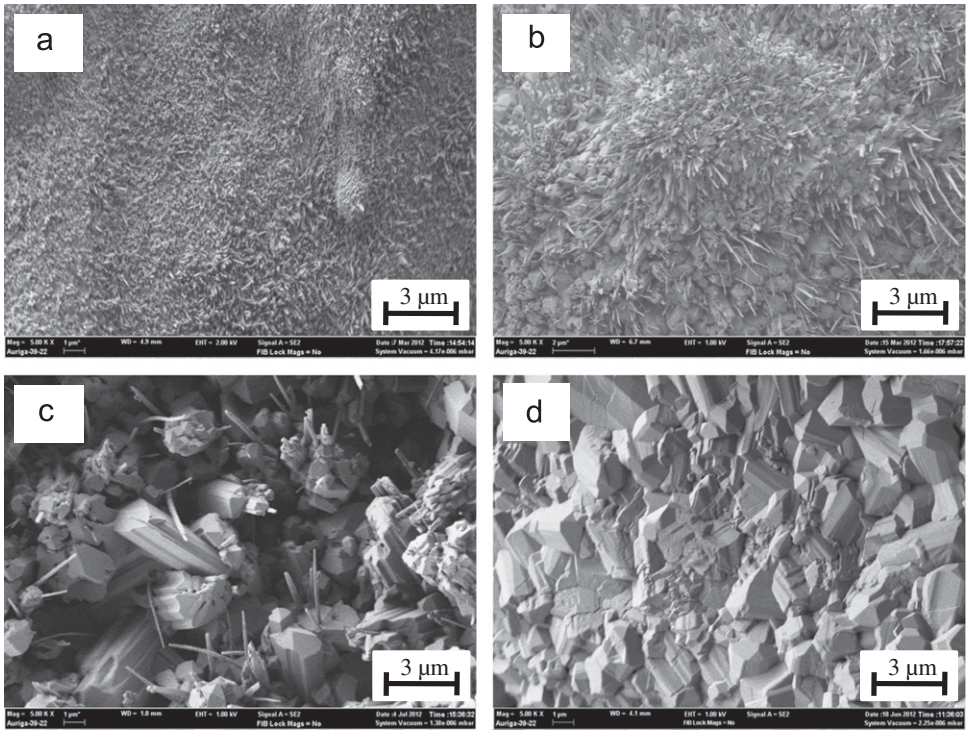

Fig. 3. FESEM micrographs of Ti64—0 h particles after thermal oxidation for 8 h with 40 ppm of oxygen flow at (a) 700 °C, (b) 750 °C, (c) 850 °C, and (d) 900 °C.

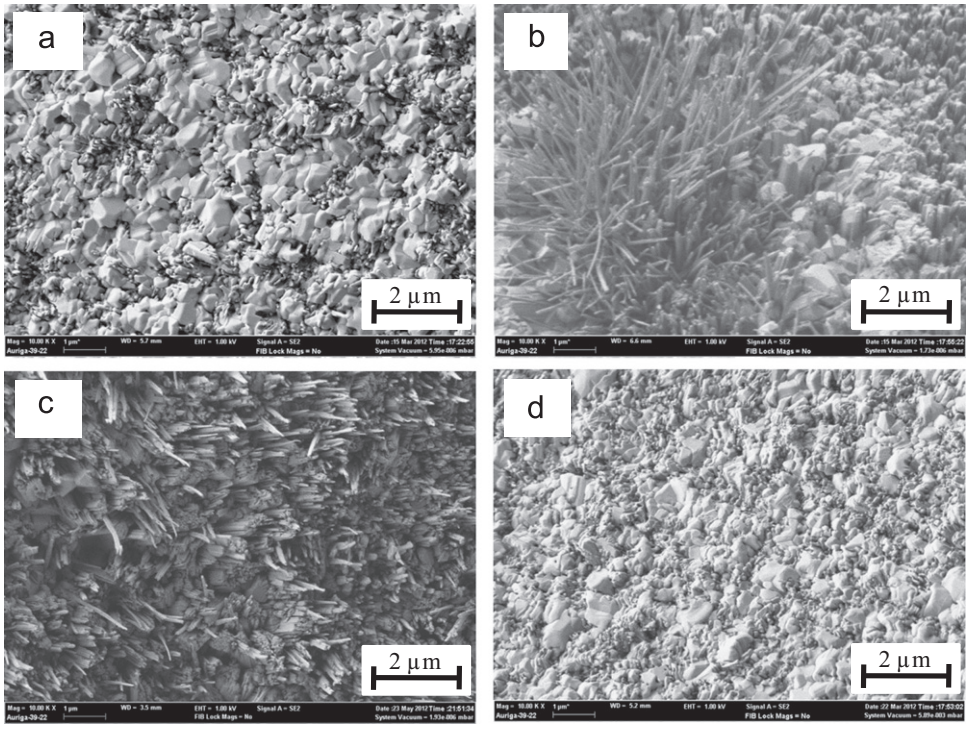

Fig. 4. FESEM micrographs of Ti64—0 h particles after thermal oxidation for 8 h at 750 °C with (a) 20 ppm, (b) 40 ppm, (c) 60 ppm and (d) 80 ppm oxygen flow.

observed on the Ti64—20 h sample (Fig. 5(d)). Thus, milling of the particles prior to oxidation is advantageous for nanowire growth.

Based on the above results, the optimum oxidation conditions for nanowire growth are 750 °C with 40 ppm O_2 flow after 20 h of milling. The nanowires grown under

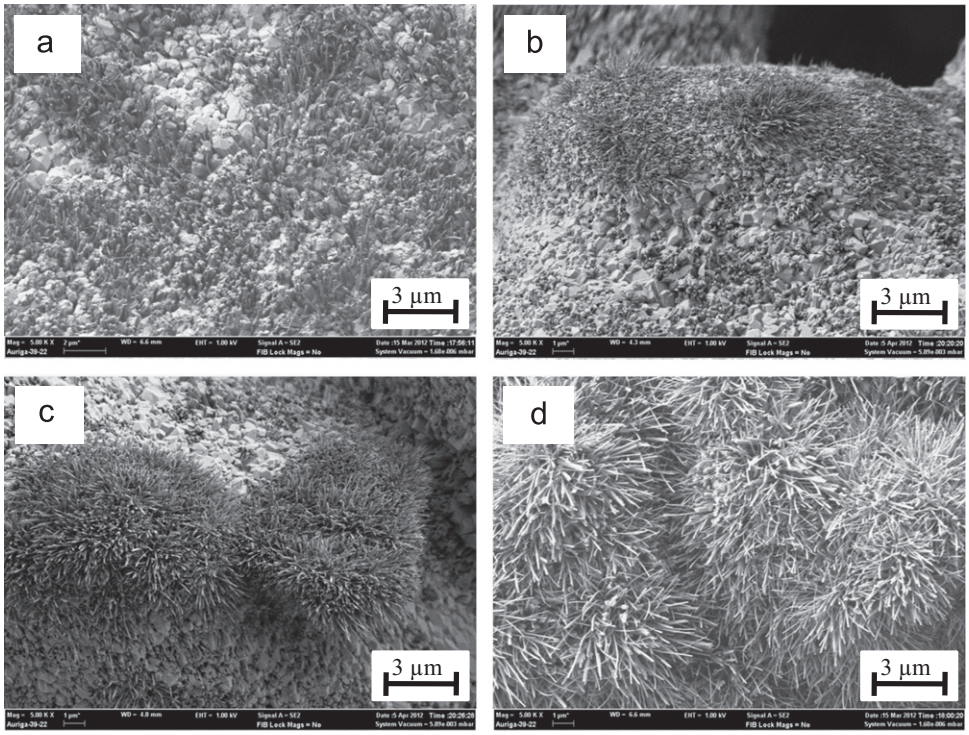

Fig. 5. FESEM micrographs of Ti64 particles after thermal oxidation for 8 h at 750 °C with 40 ppm oxygen flow: (a) Ti64—0 h, (b) Ti64—10 h, (c) Ti64—15 h and (d) Ti64—20 h.

these conditions were investigated under high magnification by FESEM as shown in Fig. 6(a). The nanowires grew with a more or less rectangular cross sectional shape with an average dimension of 20–40 nm across. The length of the nanowires varied from 2 to 3 μm. The crystal structure of the resulting oxide was obtained by XRD as shown in Fig. 6(b). The rutile phase of TiO_2 was observed along with α-Ti and α-Al_2O_3 peaks. These results are consistent with the relevant literature for Ti64 where α-Al_2O_3 is a known oxidation byproduct [44]. FESEM analysis was performed on the Ti64—20 h sample after oxidation at 750 °C in 20 ppm of oxygen flow (Fig. 6(c)). EDS area analysis on this sample at different positions showed the presence of Al in the oxides with Ti, O and V peaks (Fig. 6(d)–(e)).

Compared with other methods for the production of TiO_2 nanostructures, the process of thermal oxidation yields several advantages most notable of which is the easy scaling for mass production. The mechanism(s) promoting the confinement to 1-D growth of TiO_2 nanowires is still under investigation. An increase in nanowire coverage after milling strongly suggests that the stress state of the metal prior to oxidation is of critical importance. Nanowire growth in the present study may be driven by the relaxation of stress similar to the mechanism reported by Kumar et al. [39] to explain CuO nanowire growth. A stress-induced growth mechanism of whiskers was first proposed by Eshelby [45]. In this theory, energy required to form a fresh surface is provided by the interaction of metal with the surrounding atmosphere. A stressed surface releases its residual stress by creating new surfaces such as nanowires. In the case of copper, fine grained underlying oxide layers prompt the outward diffusion of Cu atoms for growing nanowires [40]. In the present case, the increased nanowire coverage observed in the samples subjected to increasing doses of milling (Fig. 5) is a possible evidence of a stress-induced growth mechanism. An increase in milling time is likely to induce more stress in the Ti64 particles. Thus, the increase in nanowire coverage may be attributed to the particle's residual stress state resulting from ball milling.

The residual stress near the particle's surface was evaluated based on the XRD-$\sin^2\psi$ technique [41–43]. To determine the surface profile and to select a suitable peak for residual stress measurement, the particles were scanned in 2θ region from 30° to 90° as shown in Fig. 7. Both α (hexagonal closed packed) and β (body centered cubic) phases of Ti were present in the as-received and milled particles. As the milling duration increased, the diffraction peaks became shorter and wider. Broadening of peaks is a possible evidence of an accumulation of stress in the Ti64—20 h sample, but can also be related to the particle size reduction. As a criterion to determine the residual stress using the XRD-$\sin^2\psi$ technique, the selection of diffraction peak should have the following characteristics [46,47]:

1. The diffraction peak should be higher in Bragg angle (2θ). Typically residual stress is measured by the Bragg angles that occur at more than 130°. In this experiment, the intensities of the peaks were very insignificant when $2\theta > 80°$. For this reason, peaks that occurred below 80° in 2θ angle were considered to calculate the residual stress.

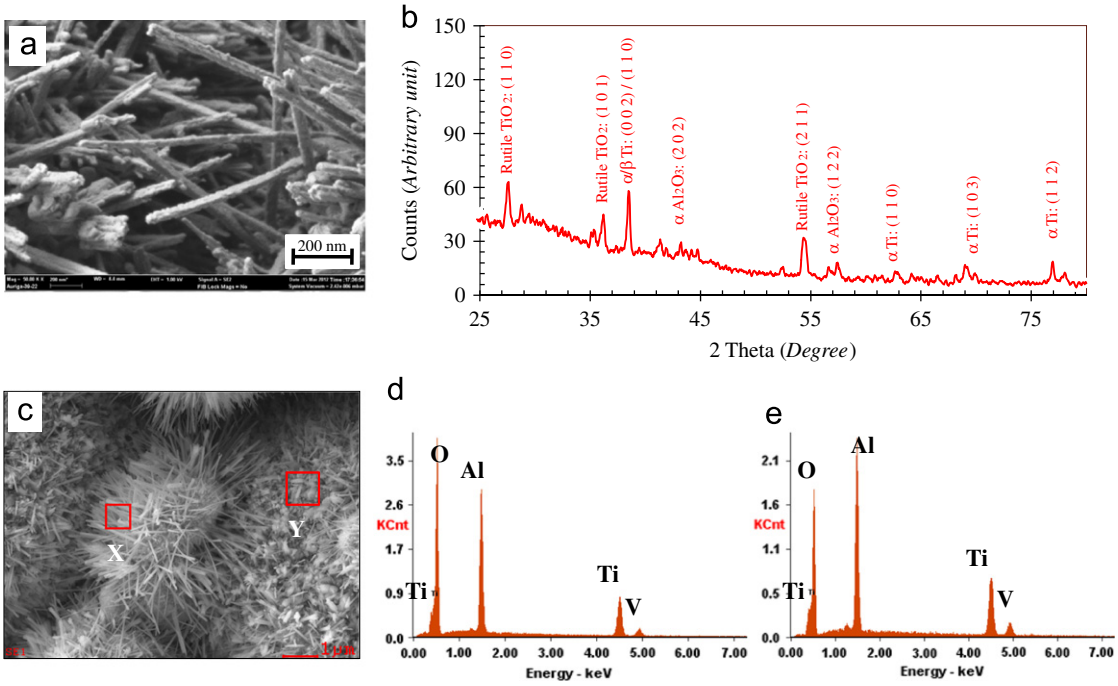

Fig. 6. (a) FESEM micrograph of the Ti64—20 h sample after oxidation in optimal conditions, (b) X-ray diffraction peaks corresponding to (a), (c) low magnification micrograph of the sample used for EDS analysis, (d) EDS spectrum taken at position 'X' and (e) EDS spectrum taken at position 'Y' in (c).

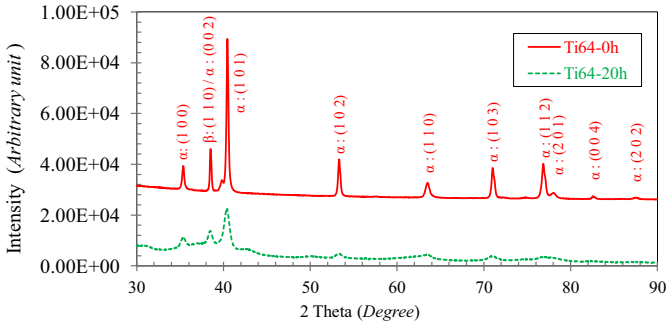

Fig. 7. X-ray diffraction (XRD) peaks of Ti64—0 h and Ti64—20 h particles.

2. The selected diffraction peak should not overlap with other diffraction peaks. For example, in Fig. 7 the diffraction peaks that occur at approximately 77° and 78° in the Ti64—0 h sample overlap in the Ti64—20 h sample. For this reason, peaks in this region were not selected for residual stress analysis.
3. The diffraction peak should be single and well shaped with high intensity. The peak from the (103) crystal planes of α-Ti that occurred at approximately 71° possessed all the properties required to determine the residual stress. This peak was selected to investigate further for residual stress measurements.

The Ti64—0 h and Ti64—20 h particles were further scanned in the 2θ region from 70° to 73° at different tilt angles (ψ) with a slow scanning speed. The tilt angles were varied from 0° to 40° as shown in Fig. 8. For the Ti64—0 h sample, a peak shift was not evident at different ψ angles but was obvious for the Ti64—20 h sample. The lattice spacing (d) was plotted against $\sin^2\psi$ as shown in Fig. 8(c). The residual stress of the particles was calculated by the following formula [41–43]:

$$\sigma = \frac{E}{1+v} m \tag{1}$$

where σ is the residual stress, E the Young's modulus, υ the Poison ratio and m the slope of the 2θ–$\sin^2\psi$ curve. By considering $E = 115$ GPa, $\upsilon = 0.31$, $m = -0.002$ and 0.004 for Ti64—0 h and Ti64—20 h particles, respectively and substituting these values in Eq. (1), the residual stresses obtained for Ti64—0 h and Ti64—20 h particles were approximately −175 MPa (tensile) and +350 MPa (compressive) respectively. Residual stress determined from the XRD-$\sin^2\psi$ method can contain uncertainty caused by errors in the diffraction peak measurement, nonlinear relation between lattice spacing (d) and $\sin^2\psi$ due to the grain interactions, anisotropic elastic property of crystalline materials and instrumental setup [47,48]. Nonetheless, the estimated values show an accurate trend for the accumulation of stress in the milled samples. It is noted that Ti64—20 h particles were subjected to 20 h of milling and had the highest coverage of nanowires. The XRD analysis indicates the accumulation of stress in the Ti64—20 h sample through peak broadening. As such, stress induced growth is a plausible mechanism for the nanowire growth. However, further studies are required to prove this mechanism.

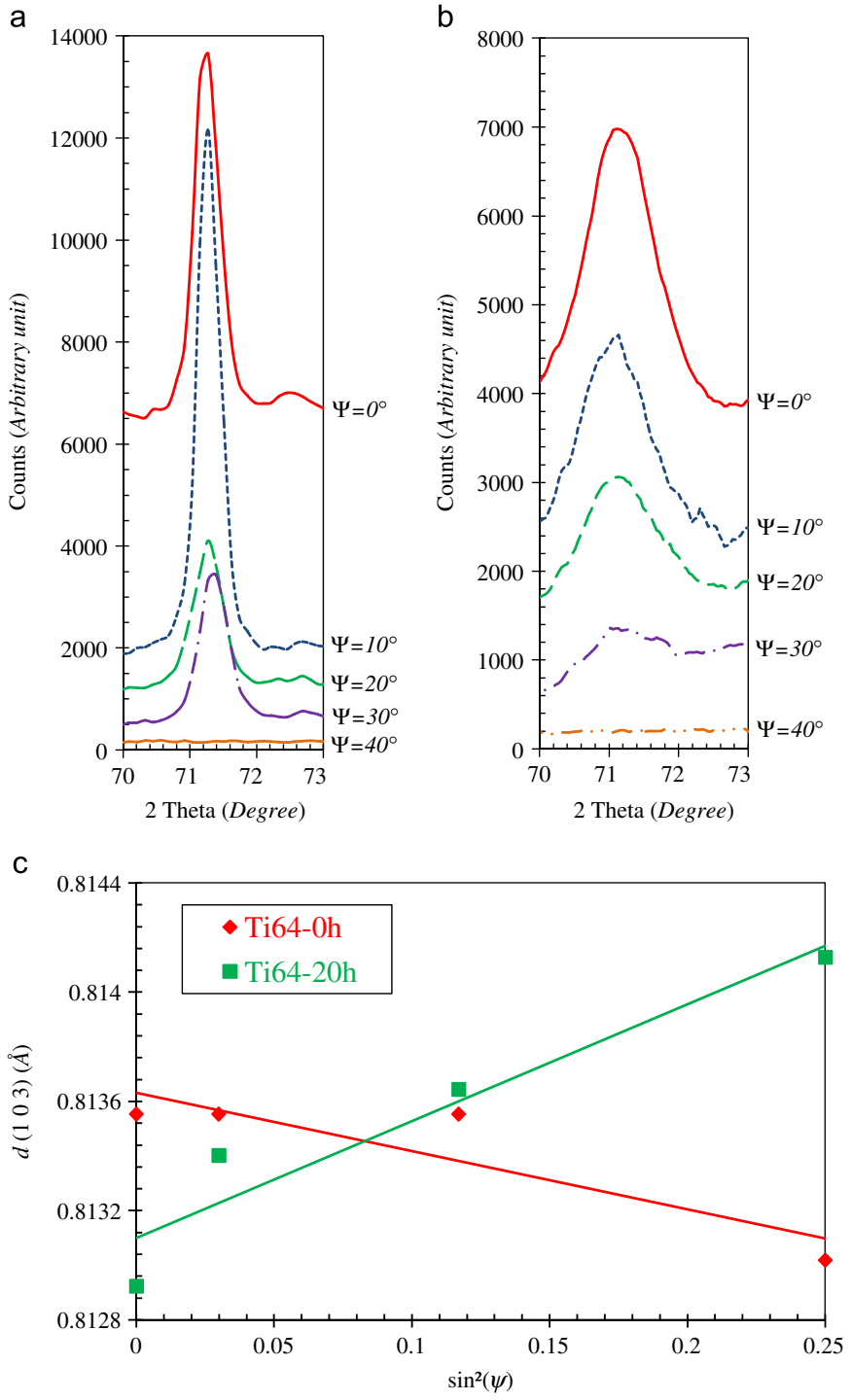

Fig. 8. (a) XRD peak of (103) plan in Ti64—0 h sample, (b) XRD peak of (103) plan in Ti64—20 h sample and (c) d–$\sin^2\psi$ plot for the Ti64—0 h and Ti64—20 h particles.

To confirm the observed effects of stress on nanowire growth, a Ti64 sheet having dimensions of 25 mm × 3 mm × 1 mm was hammered at one end until the compressive strain value of 0.6 of the original sample thickness was achieved. The other end was unchanged, resulting in zero strain at this un-hammered end. This nonuniform deformation resulted in a stress gradient along the length of the sheet as can be seen in Fig. 9(a). Oxidation was carried out at 750 °C for 8 h with 40 ppm oxygen flow. After oxidation, the Ti64 sheet was characterized by FESEM at different positions as shown in Fig. 9(b)–(e). As can be seen from Fig. 9(b), no nanowires were observed at the un-hammered end (position 1). The surface was occupied by faceted grains. At position 2, the formation of some nanowires was seen (Fig. 9(c)). Nanowire coverage was further increased at position 3, where the strain reached a value of 0.3 (Fig. 9(d)). Finally, the highest coverage

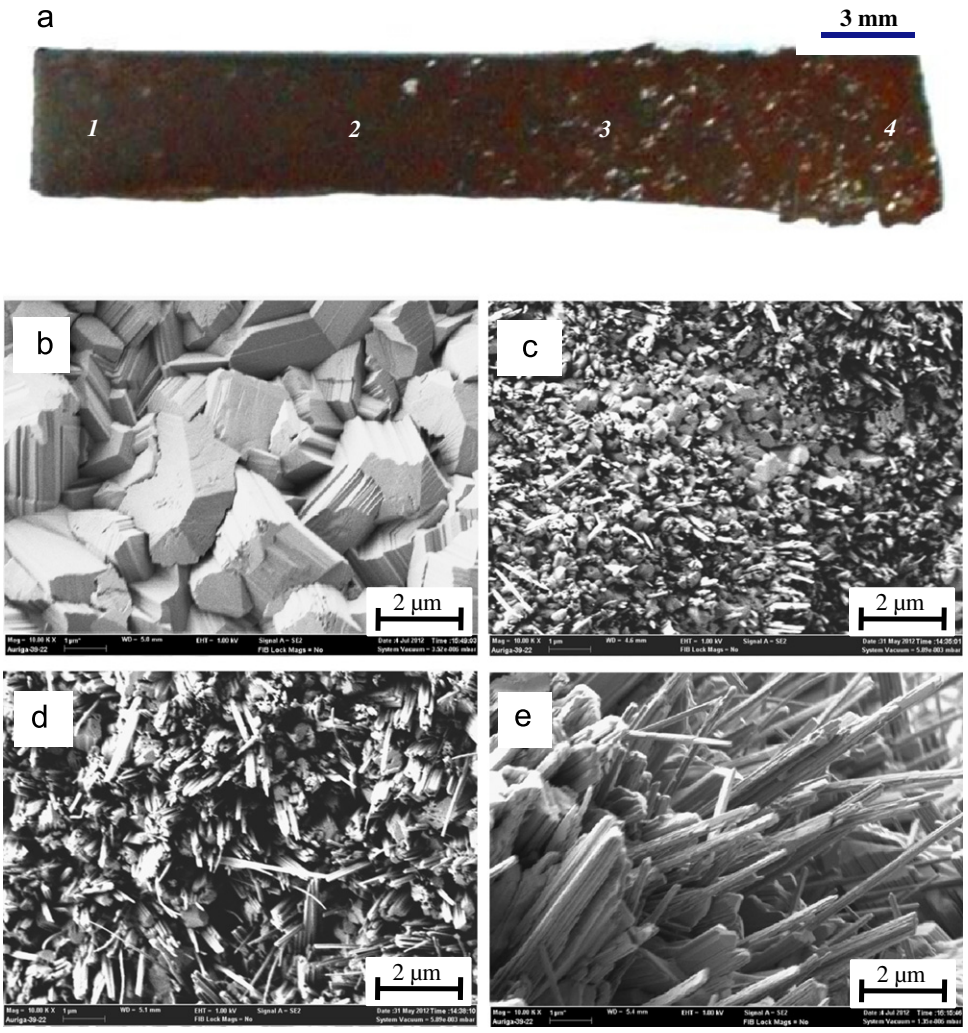

Fig. 9. (a) Ti64 sheet (25 mm × 3 mm × 1 mm), and FESEM micrograph on the Ti64 sheet at (b) position 1, (c) position 2, (d) position 3 and (e) position 4.

of nanowires was found at position 4 (Fig. 9(e)), where the strain was maximum and calculated to be 0.6. The nanowire coverage increased along the induced stress gradient. Thus, stress clearly plays a significant role in the induced growth of TiO_2 nanowires.

Stress induced nanowire growth by thermal oxidation is an easy, novel and inexpensive way to produce 1-D TiO_2 nanowires. In addition, this method also facilitates the growth of nanowires directly on a given Ti substrate. The oxidative growth process results in crystalline nanowires that have potential for engineering applications. The results presented here show that induced stress clearly enhanced the coverage of nanowires on Ti64 particles. Further studies are required to better explain the stress-induced growth mechanism for the production of TiO_2 nanowires by thermal oxidation.

4. Conclusions

From the experimental work described in this paper, the following conclusions can be drawn:

1. TiO_2 nanowires can be grown on Ti64 particles by thermal oxidation.
2. The growth of TiO_2 nanowires is sensitive to temperature, oxygen concentration, and stress state of the Ti64 substrate. The optimum growth condition for TiO_2 nanowires in this study was found to be 750 °C with 40 ppm of oxygen flow.
3. The resultant TiO_2 nanowires are crystalline and possess the rutile phase of TiO_2.
4. Stress enhances the growth of TiO_2 nanowires on Ti64 alloys. With increasing stress, a higher coverage of nanowires was observed on the Ti64 particles and metal sheets.

Acknowledgments

The authors acknowledge the financial support of High Impact Research Grant (HIR, Project no. UM.C/625/1/HIR/040) from the University of Malaya.

References

[1] A.K. Mahapatra, Synthesis of quantum-confined CdS nanotubes, Journal of Nanoparticle Research 11 (2009) 467–475.

[2] M.M.G. Alemany, L. Tortajada, X.Y. Huang, M.L. Tiago, L.J. Gallego, J.R. Chelikowsky, Role of dimensionality and quantum confinement in p-type semiconductor indium phosphide quantum dots, Physical Review B 78 (23) (2008) 233101.

[3] P.J. Poole, J. Lefebvre, J. Fraser, Spatially controlled, nanoparticle-free growth of InP nanowires, Applied Physics Letters 83 (10) (2003) 2055–2057.

[4] P. Keller, H. Ferkel, K. Zweiacker, J. Naser, J.U. Meyer, W. Riehemann, The application of nanocrystalline $BaTiO_3$-composite films as CO_2-sensing layers, Sensors and Actuators B—Chemical 57 (1-3) (1999) 39–46.

[5] Y.J. Hwang, A. Boukai, P.D. Yang, High density n-Si/n-TiO_2 core/shell nanowire arrays with enhanced photoactivity, Nano Letters 9 (1) (2009) 410–415.

[6] M. Shafiei, J. Yu, R. Arsat, K. Kalantar-zadeh, E. Comini, M. Ferroni, G. Sberveglieri, W. Wlodarski, Reversed bias Pt/nanostructured ZnO Schottky diode with enhanced electric field for hydrogen sensing, Sensors and Actuators B—Chemical 146 (2) (2010) 507–512.

[7] H.W. Peng, J.B. Li, Quantum confinement and electronic properties of rutile TiO_2 nanowires, Journal of Physical Chemistry C 112 (51) (2008) 20241–20245.

[8] P.V. Avramov, D.G. Fedorov, P.B. Sorokin, L.A. Chernozatonskii, S.G. Ovchinnikov, Quantum dots embedded into silicon nanowires effectively partition electron confinement, Journal of Applied Physics 104 (5) (2008) 054305.

[9] E.D. Herderick, J.S. Tresback, A.L. Vasiliev, N.P. Padture, Template-directed synthesis, characterization and electrical properties of Au–TiO_2–Au heterojunction nanowires, Nanotechnology 18 (15) (2007) 155204.

[10] Y. Huang, X.F. Duan, Y. Cui, C.M. Lieber, Gallium nitride nanowire nanodevices, Nano Letters 2 (2) (2002) 101–104.

[11] Y.L. Chueh, C.H. Hsieh, M.T. Chang, L.J. Chou, C.S. Lao, J.H. Song, J.Y. Gan, Z.L. Wang, RuO_2 nanowires and RuO_2/TiO_2 core/shell nanowires: from synthesis to mechanical, optical, electrical, and photoconductive properties, Advanced Materials 19 (2007) 143–149.

[12] E. Comini, G. Faglia, G. Sberveglieri, Z. Pan, Z.L. Wang, Stable and highly sensitive gas sensors based on semiconducting oxide nanobelts, Applied Physics Letters 81 (10) (2002) 1869–1871.

[13] D. Kim, A. Ghicov, S.P. Albu, P. Schmuki, Bamboo-type TiO_2 nanotubes: improved conversion efficiency in dye-sensitized solar cells, Journal of American Chemical Society 130 (49) (2008) 16454–16455.

[14] S.H. Kang, J.Y. Kim, Y. Kim, H.S. Kim, Y.E. Sung, Surface modification of stretched TiO_2 nanotubes for solid-state dye-sensitized solar cells, Journal of Physical Chemistry C 111 (26) (2007) 9614–9623.

[15] D.A. Wang, Y. Liu, C.W. Wang, F. Zhou, W.M. Liu, Highly flexible coaxial nanohybrids made from porous TiO_2 nanotubes, ACS Nano 3 (5) (2009) 1249–1257.

[16] D.A. Wang, T.C. Hu, L.T. Hu, B. Yu, Y.Q. Xia, F. Zhou, W.M. Liu, Microstructured arrays of TiO_2 nanotubes for improved photoelectrocatalysis and mechanical stability, Advanced Functional Materials 19 (12) (2009) 1930–1938.

[17] S. Meng, J. Ren, E. Kaxiras, Natural dyes adsorbed on TiO_2 nanowire for photovoltaic applications: enhanced light absorption and ultrafast electron injection, Nano Letters 8 (10) (2008) 3266–3272.

[18] M. Paulose, K. Shankar, O.K. Varghese, G.K. Mor, B. Hardin, C.A. Grimes, Backside illuminated dye-sensitized solar cells based on titania nanotube array electrodes, Nanotechnology 17 (5) (2006) 1446–1448.

[19] S.K. Mohapatra, M. Misra, Enhanced photoelectrochemical generation of hydrogen from water by 2, 6-dihydroxyantraquinone-functionalized titanium dioxide nanotubes, Journal of Physical Chemistry C 111 (2007) 11506–11510.

[20] G.K. Mor, H.E. Prakasam, O.K. Varghese, K. Shankar, C.A. Grimes, Vertically oriented Ti–Fe–O nanotube array films: toward a useful material architecture for solar spectrum water photoelectrolysis, Nano Letters 7 (8) (2007) 2356–2364.

[21] C.M. Carney, S. Yoo, S.A. Akbar, TiO_2–SnO_2 nanostructures and their H_2 sensing behavior, Sensors and Actuators B 108 (2005) 29–33.

[22] O.K. Varghese, D. Gong, M. Paulose, K.G. Ong, C.A. Grimes, Hydrogen sensing using titania nanotubes, Sensors and Actuators B 93 (2003) 338–344.

[23] K. Shin, S.I. Seok, S.H. Im, J.H. Park, CdS or CdSe decorated TiO_2 nanotube arrays from spray pyrolysis deposition: use in photoelectrochemical cells, Chemical Communications 46 (2010) 2385–2387.

[24] J.M. Macak, C. Zollfrank, B.J. Rodriguez, H. Tsuchiya, M. Alexe, P. Greil, P. Schmuki, Ordered ferroelectric lead titanate nanocellular structure by conversion of anodic TiO_2 nanotubes, Advanced Materials 21 (2009) 3121–3125.

[25] A.W. Tan, B. Pingguan-Murphy, R. Ahmad, S.A. Akbar, Review of titania nanotubes: fabrication and cellular response, Ceramics International 38 (2012) 4421–4435.

[26] L. Tang, Y. Tian, Y. Liu, Z. Wang, B. Zhou, One-step solution synthesis of urchin-like ZnO superstructures from ZnO rods, Ceramics International 39 (3) (2013) 2303–2308.

[27] C.S. Rout, G.U. Kulkarni, C.N.R. Rao, Room temperature hydrogen and hydrocarbon sensors based on single nanowires of metal oxides, Journal of Physics D: Applied Physics 40 (9) (2007) 2777–2782.

[28] C.-H. Han, D.-W. Hong, I.-J. Kim, J. Gwak, S.-D. Han, K.C. Singh, Synthesis of Pd or Pt/titanate nanotube and its application to catalytic type hydrogen gas, Sensors and Actuators B—Chemical 128 (2007) 320–325.

[29] O. Landau, A. Rothschild, E. Zussman, Processing–microstructure–properties correlation of ultrasensitive gas sensors produced by electrospinning, Chemistry of Materials 21 (1) (2009) 9–11.

[30] W. Biao, Z.Y. Dong, H.L. Ming, C.J. Sheng, G.F. Li, L. Yun, W.L. Jun, Improved and excellent CO sensing properties of Cu-doped TiO_2 nanofibers, Chinese Science Bulletin 55 (3) (2010) 228–232 2010.

[31] H. Li, L. Cao, W. Liu, G. Su, B. Dong, Synthesis and investigation of TiO_2 nanotube arrays prepared by anodization and their photocatalytic activity, Ceramics International 38 (2012) 5791–5797.

[32] A. Hu, C. Cheng, X. Li, J. Jiang, R. Ding, J. Zhu, F. Wu, J. Liu, X. Huang, Two novel hierarchical homogeneous nanoarchitectures of TiO_2 nanorods branched and P25-coated TiO_2 nanotube arrays and their photocurrent performances, Nanoscale Research Letters 6 (91) (2011) 2–6.

[33] H.F. Lu, F. Li, G. Liu, Z.-G. Chen, D.-W. Wang, H.-T. Fang, G.Q. Lu, Z.H. Jiang, H.-M. Cheng, Amorphous TiO_2 nanotube arrays for low-temperature oxygen sensors, Nanotechnology 19 (2008) 405504.

[34] M. Paulose, O.K. Varghese, G.K. Mor, C.A. Grimes, K.G. Ong, Unprecedented ultra-high hydrogen gas sensitivity in undoped titania nanotubes, Nanotechnology 17 (2006) 398–402.

[35] S. Yoo, S.A. Akbar, K.H. Sandhage, Nanocarving of titania (TiO_2): a novel approach for fabricating chemical sensing platform, Ceramics International 30 (7) (2004) 1121–1126.

[36] L. Francioso, A.M. Taurino, A. Forleo, P. Siciliano, TiO_2 nanowires array fabrication and gas sensing properties, Sensors and Actuators B—Chemical 130 (2008) 70–76.

[37] H. Lee, S. Dregia, S. Akbar, M. Alhoshan, Growth of 1-D TiO_2 nanowires on Ti and Ti alloys by oxidation, Journal of Nanomaterials 2010 (2010) 503186 (7 pp.).

[38] B. Dinan, S.A. Akbar, One-dimensional oxide nanostructures produced by gas phase reaction, Functional Materials Letters 2 (3) (2009) 87–94.

[39] A. Kumar, A.K. Srivastava, P. Tiwari, R.V. Nandedkar, The effect of growth parameters on the aspect ratio and number density of CuO nanorods, Journal of Physics: Condensed Matter 16 (2004) 8531–8543.

[40] R. Mema, L. Yuan, Q. Du, Y. Wang, G. Zhou, Effect of surface stresses on CuO nanowire growth in the thermal oxidation of copper, Chemical Physics Letters 512 (2011) 87–91.
[41] V.M. Hauk, in: E. Kula, V. Weiss (Eds.), Residual Stress and Stress Relaxation, Plenum Press, 1982, p. 117.
[42] B.D. Cullity, S.R. Stock, Elements of X-ray Diffraction, 3rd ed., Prentice Hall, Upper Saddle River, NJ, 2001, p. 435.
[43] M.E. Fitzpatrick, A.T. Fry, P. Holdway, F.A. Kandil, J. Shackleton, L. Suominen, Determination of residual stresses by X-ray diffraction—Issue 2, DTI, Measurement Good Practice Guide No. 52, 2005.
[44] H.L. Du, P.K. Datta, D.B. Lewis, J.S. Burnell-Gray, Air oxidation behavior of Ti–6Al–4V alloy between 650 and 850°, Corrosion Science 36 (4) (1994) 631–642.
[45] J.D. Eshelby, A tentative theory of metallic whisker growth, Physical Review 91 (3) (1953) 755–756.
[46] X. Zheng, J. Li, Y. Zhou, X-ray diffraction measurement of residual stress in PZT thin films prepared by pulsed laser deposition, Acta Materialia 52 (2004) 3313–3322.
[47] Q. Luo, A.H. Jones, High-precision determination of residual stress of polycrystalline coatings using optimised XRD-$\sin^2\psi$ technique, Surface and Coatings Technology 205 (2010) 1403–1408.
[48] P.S. Prevey, in: J. Friel, Vander Voort (Eds.), Current Applications Of Xrd Diffraction Residual Stress Measurement, Development in Materials Characterization Technologies, ASM International, Materials Park, OH, 1996 103–110.